Control and Manipulation of Gold Nanocatalysis: Effects of Metal Oxide Support Thickness and Composition

7 AUTHORS, INCLUDING:

Ueli Heiz
Technische Universität München
90 PUBLICATIONS 4,465 CITATIONS

Bokwon Yoon
Georgia Institute of Technology
38 PUBLICATIONS 2,793 CITATIONS

Uzi Landman
Georgia Institute of Technology
488 PUBLICATIONS 23,538 CITATIONS

Article

Control and Manipulation of Gold Nanocatalysis: Effects of Metal Oxide Support Thickness and Composition

Chris Harding, Vahideh Habibpour, Sebastian Kunz, Adrian Nam-Su Farnbacher, Ueli Heiz, Bokwon Yoon, and Uzi Landman

More About This Article

Additional resources and features associated with this article are available within the HTML version:

- Supporting Information
- Access to high resolution figures
- Links to articles and content related to this article
- Copyright permission to reproduce figures and/or text from this article
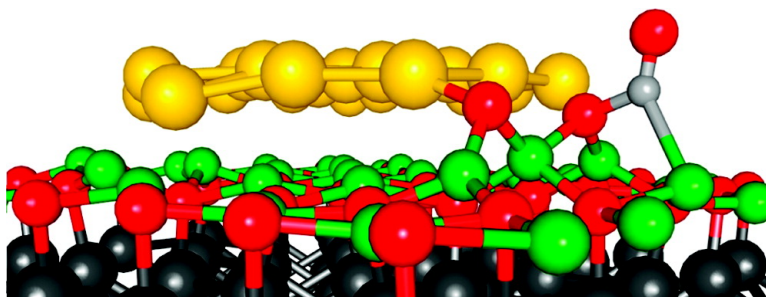
View the Full Text HTML

Control and Manipulation of Gold Nanocatalysis: Effects of Metal Oxide Support Thickness and Composition

Chris Harding,[†] Vahideh Habibpour,[†] Sebastian Kunz,[†]
Adrian Nam-Su Farnbacher,[†] Ueli Heiz,*,[†] Bokwon Yoon,[‡] and Uzi Landman*,[‡]

*Lehrstuhl für Physikalische Chemie, Technische Universität München, Lichtenbergstrasse 4,
85748 Garching, Germany, and School of Physics, Georgia Institute of Technology,
Atlanta, Georgia 30332-0430*

Received June 26, 2008; E-mail: ulrich.heiz@mytum.de; uzi.landman@physics.gatech.edu

Abstract: Control and tunability of the catalytic oxidation of CO by gold clusters deposited on MgO surfaces grown on molybdenum, Mo(100), to various thicknesses are explored through temperature-programmed reaction measurements on mass-selected 20-atom gold clusters and via first-principles density functional theory calculations. Au_{20} was chosen because in the gas phase it is characterized as an extraordinarily stable tetrahedral-pyramidal structure. Dependencies of the catalytic activities and microscopic reaction mechanisms on the thickness and stoichiometry of the MgO films and on the dimensionalities and structures of the adsorbed gold clusters are demonstrated and elucidated. Langmuir−Hinshelwood mechanisms and reaction barriers corresponding to observed low- and high-temperature CO oxidation reactions are calculated and analyzed. These reactions involve adsorbed O_2 molecules that are activated to a superoxo- or peroxo-like state through partial occupation of the antibonding orbitals. In some cases, we find activated, dissociative adsorption of O_2 molecules, adsorbing at the cluster peripheral interface with the MgO surface. The reactant CO molecules either adsorb on the MgO surface in the cluster proximity or bind directly to the gold cluster. Along with the oxidation reactions on stoichiometric ultrathin MgO films, we also study reactions catalyzed by Au_{20} nanoclusters adsorbed on relatively thick defect-poor MgO films supported on Mo and on defect-rich thick MgO surfaces containing oxygen vacancy defects.

Introduction

One of the principal goals of modern research in chemical catalysis is the development of methods for further control and manipulation of the activity, selectivity, and specificity of catalytic systems.[1,2] This can be achieved in various ways, including (i) selection of the catalyst material and composition, (ii) manipulations of the atomic structure, morphology, and shape of the catalyst, (iii) choice of the support (composition, structure, and thickness[3,4]), and (iv) the use of externally applied electric or electromagnetic fields.[5] Particle size plays an important role in determining the chemical reactivity of material aggregates. A main endeavor in current catalytic research aims at characterizing, understanding, controlling, and utilizing the effects of the particle size on catalytic properties. With this in mind, each of the aforementioned ways of controlling and modifying catalytic activity may be explored also in conjunction with variations of the size of the catalytic particles under investigation. Indeed, numerous studies have demonstrated, for a broad range of size scales, dependencies of, and correlations

between, the catalytic properties and the size or dimensionality of the catalytic material. For example, it has been shown[6] that for a number of reactions the catalytic activity of single-crystal surfaces can be modified by using metal nanoparticles with an average size down to a few nanometers. In this size range, it was found that nanocrystallites of different size may exhibit different structural motifs characterized by different proportions of exposed crystallographic facets (with corresponding different chemical reactivities), thus resulting in size-dependent variations of the catalytic activity of the nanocrystallites.[6−8]

Moreover, new catalytic properties emerge that could not have been anticipated through extrapolation of the behavior known for larger sizes when the reduction of the size of metal catalyst particles reaches the ultimate nanocluster regime, that is, clusters comprised of about 10 to 20 atoms ($\leq$1 nm in "diameter"). In this size range, the nanocluster may be viewed as a quasi-"zero-dimensional" (0D) quantum dot whose physical and chemical properties are dominantly affected by quantum size effects[1,2,9−14] originating from electrons confined in a cluster of finite size (in all three dimensions), including coupling to the supporting surface. As aforementioned, in this regime, which is the one where gold clusters exhibit unique reactivities (see refs 10, 13, and 14 and the discussion below), extrapolations from larger

[†] Technische Universität München.
[‡] Georgia Institute of Technology.
(1) Heiz, U.; Landman, U. *Nanocatalysis*; Nanoscience and Technology; Springer Verlag: Berlin, 2007.
(2) Landman, U.; Yoon, B.; Zhamg, C.; Heiz, U.; Arenz, M. *Top. Catal.* **2007**, *44*, 145.
(3) Ricci, D.; Bongiorno, A.; Pacchioni, G.; Landman, U. *Phys. Rev. Lett.* **2006**, *97*, 036106.
(4) Zhang, C.; Yoon, B.; Landman, U. *J. Am. Chem. Soc.* **2007**, *129*, 2228.
(5) Yoon, B.; Landman, U. *Phys. Rev. Lett.* **2008**, *100*, 056102.

(6) Henry, C. R. *Surf. Sci. Rep.* **1998**, *31*, 231.
(7) Henry, C. R. In *Nanocatalysis*; Heiz, U., Landman, U., Eds.; Nanoscience and Technology; Springer Verlag: Berlin, 2007.
(8) Libuda, J.; Meusel, I.; Hoffmann, J.; Hartmann, J.; Piccolo, L.; Henry, C. R.; Freund, H. J. *J. Chem. Phys.* **2001**, *114*, 4669.

sizes using arguments relying on surface-to-volume ratios and scaling relations based on the enumeration of special sites (e.g., corner atoms) as a function of the size [15-17] are not operative; indeed, on this size scale, almost all of the atoms of the metal cluster are essentially surface atoms, and almost all can be classified as undercoordinated (compared to bulk). Instead, in this important regime, which is the focus of our research in this paper, one must resort to quantum mechanical calculations that highlight the correlations between the electronic structure of the coupled cluster−substrate catalytic system and the geometrical arrangement of the atoms (including their distortions in the course of reactions, which we termed as "dynamical fluctionality"[18]) on an atom-by-atom level, that is, when every atom counts and where "small is different" in an essential, i.e., nonscalable, manner. This is indeed the approach that we have taken in earlier studies[1,2,4,5,13,14,18] and the one that we use in this study.

While the utilization of reactive metals, e.g., transition metals, as well as some coinage metals (like silver, palladium, and platinum) in catalytic processes is rather common, the catalytic properties of gold are less well-known, and they remain largely unexploited; indeed, until about 2 decades ago, gold was considered to be strictly inert. While this is the case for bulk gold, when prepared as aggregates (clusters) of nanometer dimensions, gold exhibits interesting, potent, and promising catalytic activity with unique specificity and selectivity characteristics.[1,2,13,18-20] In particular, joint experiments and theoretical investigations of the catalytic oxidation of CO on size-selected gold clusters supported on relatively thick, defect-rich (F center, FC), MgO surfaces have shown low-temperature catalytic combustion to occur at temperatures as low as 140 K for Au_n clusters with $8 \leq n \leq 20$ Au atoms; that is, a nonplanar (two-layer) Au_8 nanocluster emerged as the smallest one to exhibit catalytic activity. [13]

We reemphasize here that the emergence[13] of such subnanometer-scale bilayer gold clusters (starting with the gold octamer), supported on thick metal oxide (MgO) surfaces containing oxygen vacancies (FCs), as the ones exhibiting catalytic activity, has its origin in two main factors: (i) the quantum size effect, where the confinement of the electrons (defined by the adsorbed cluster structure and dimensionality and including the charging effect from the surface defects) serves to determine the positioning of the chemically active energy levels (in particular, the location of sd orbitals of gold lying

near the Fermi level; see the discussion in refs 13 and 14 and illustrative comparisons, given in ref 18 between the electronic density of states of surface-supported Au_3, Au_4, and Au_8 clusters, as well as of a doped Au_3Sr cluster, with and without an adsorbed O_2 molecule), and (ii) the cluster proximity effect, where the distances between the adsorbed reactant molecules are restricted by the nanometer (or subnanometer) size of the cluster, thus lowering (concomitantly with the optimal positioning of energy levels noted above and charge-induced activation) the enthalpic and entropic reaction activation barriers.

It is pertinent to remark here that most recent aberration-corrected transmission electron microscopy investigations[21] used for identification of the active catalytic gold species among the many present on real catalysts have found that the high catalytic activity for CO oxidation is unambiguously correlated with the presence of bilayer clusters (supported on a metal oxide) that are less than 1 nm in diameter and contain on the order of only 10 Au atoms. Interestingly, these studies, which are fully consistent with the early theoretical and experimental investigations described above,[13,14,18] found that the catalytically active subnanometer gold bilayer clusters represented only $1.05 \pm 0.72\%$ of the total Au loading, with the remaining 98.82 ± 0.8 atomic % of Au being larger particles. The authors further emphasized their findings by stating that "The observation that the active species in our Au/FeO$_x$ catalysts consist of subnanometer clusters differs from numerous earlier investigations that identified 2- to 5-nm particles as the critical nanostructures". The authors also remarked about experimental difficulties in detecting these subnanometer clusters, stating that "...it is probable that these minority Au species would not be easily detected with traditional 'bulk' techniques such as extended x-ray absorption fine structure or Mossbauer spectroscopy, or even by surface analysis techniques such as x-ray photoelectron spectroscopy (XPS), because their contribution to the total signal would be minimal compared with that of the larger nanoparticles".

In the earlier theoretical investigations,[13,14,18] charging of the adsorbed metal cluster through partial electron transfer from the oxygen vacancy FC defects (or other Lewis basic defect sites) was found to play a key role in anchoring of the gold cluster to the metal oxide (MgO) surface (thus enhancing the stability of the adsorbed gold nanoclusters against coalescence and sintering) and in the activation and promotion of the reactant molecules. The change of the charge state of the cluster (through charge transfer from the underlying substrate, causing an upward shift of the cluster energy levels and enhanced population near the Fermi level) and consequent occupation of the antibonding $2\pi^*$ orbital of O_2 (which, upon adsorption of the O_2 molecule on the cluster, drops below the Fermi level, E_F, of the supported gold nanocluster and mixes with the sd states near E_F) lead to activation of the O−O bond and have been identified as underlying the catalytic activity.[2,10,13,14,18] The unusual activation of oxygen upon adsorption is portrayed in the elongation of $d(\text{O−O})$ to about 1.35 Å, corresponding to a superoxo-like state, or to $d(\text{O−O}) > 1.4$ Å, corresponding to a peroxo-like state. Interestingly, in most oxidation (combustion) reactions catalyzed by gold nanoclusters, the O_2 molecule is activated through its interaction with the gold nanocluster but does not dissociate, whereas for reactions catalyzed on extended metal surfaces, dissociation of the adsorbed O_2 molecules is the common route to oxidation reactions.

(9) Abbet, S.; Sanchez, A.; Heiz, U.; Schneider, W. D. *J. Catal.* **2001**, *198*, 122.

(10) Heiz, U.; Bernhardt, T. M.; Landman, U. In *Nanocatalysis*; Heiz, U.; Landman, U., Eds.; Nanoscience and Technology; Springer Verlag: Berlin, 2007.

(11) Heiz, U.; Sanchez, A.; Abbet, S.; Schneider, W. D. *J. Am. Chem. Soc.* **1999**, *121*, 3214.

(12) Judai, K.; Abbet, S.; Wörz, A. S.; Heiz, U.; Henry, C. R. *J. Am. Chem. Soc.* **2004**, *126*, 2732.

(13) Sanchez, A.; Abbet, S.; Heiz, U.; Schneider, W. D.; Hakkinen, H.; Barnett, R. N.; Landman, U. *J. Phys. Chem. A* **1999**, *103*, 9573.

(14) Yoon, B.; Landman, U.; Wörz, A.; Antonietti, J.-M.; Abbet, S.; Judai, K.; Heiz, U. *Science* **2005**, *307*, 403.

(15) Hvolbaek, B.; Janssens, T. V. W.; Clausen, B. S.; Falsig, H.; Christensen, C. H.; Norskov, J. K. *Nanotoday* **2007**, *2*, 14.

(16) Janssens, T. V. W.; Clausen, B. S.; Hvolbaek, B.; Falsig, H.; Christensen, C. H.; Bligaard, C. H.; Norskov, J. K. *Top. Catal.* **2007**, *44*, 15.

(17) Falsig, H.; Hvolbaek, B.; Kristensen, I. S.; Jiang, T.; Bligaard, C. H.; Norskov, J. K. *Angew. Chem., Int. Ed.* **2008**, *47*, 4835.

(18) Häkkinen, H.; Abbet, S.; Sanchez, A.; Heiz, U.; Landman, U. *Angew. Chem., Int. Ed.* **2003**, *42*, 1297.

(19) Haruta, M. *Catal. Today* **1997**, *36*, 153.

(20) Valden, M.; Lai, X.; Goodman, D. W. *Science* **1998**, *281*, 1647.

(21) Herzing, A. A.; Kiely, C. J.; Carley, A. F.; Landon, P.; Hutchings, G. J. *Science* **2008**, *321*, 1331.

Another key factor that influences the catalytic activity of gold nanoclusters is their ability to distort in the course of interaction with the reactants. This property has been termed "dynamical fluctionality", and it is unique to clusters in the nanometer size range.[18] Such structural fluctional distortions enable adsorption and activation of the reactants, as well as lower the activation barriers of reactions between the adsorbed reactants.

Recently, it has been predicted theoretically[3,4] and confirmed experimentally[22] that a dimensionality crossover will occur for gold clusters deposited on thin metal oxide films grown on appropriate metal surfaces [e.g., MgO grown on Mo(100) or Ag(100)] as a function of the metal oxide film thickness. Thinner MgO films with less than seven to eight layers were predicted (and subsequently found experimentally) to favor two-dimensional (2D) wetting gold island structures, whereas on thicker films the dimensionalities of the free clusters are maintained. Stabilization of the 2D structures has been shown to be caused by the accumulation of excess electronic charge, originating from the underlying metal, at the cluster interface with the MgO film. This has been predicted[4] to result in the catalytic activity of gold nanoclusters adsorbed on thin MgO films, even when the films have no Lewis basic defect sites (e.g., FCs), provided that the films are thin enough.

The experimental and theoretical investigations presented herein aim at demonstrating the effect of the metal oxide film thickness on the catalytic activity and reaction mechanisms of adsorbed gold nanoclusters (in particular, Au_{20}). We indeed show that sufficiently thin MgO films can serve as supports in gold nanocatalysis, even when they do not contain Lewis basic defect sites, and identify low- and high-temperature reaction channels. We also contrast these results with catalytic CO oxidation on thick, defect-rich MgO films. Conceptually, we show the active site on the cluster to be characterized by enhanced electron density, which activates (or, less often, dissociates) the adsorbed O_2 molecule and promotes the bonding of CO. The location and extent of the enhanced charge density depend on the characteristics of the underlying metal oxide.

Methods

a. Experimental Methods. The model catalytic systems used in these investigations consist of Au_{20} clusters adsorbed on metal oxide [MgO(100)] films of various thicknesses and stoichiometries (that is, with and without oxygen vacancies) supported on Mo(100). The Mo(100) single crystal was cleaned and a film of MgO was grown on it by the evaporation of Mg metal in a background of O_2 at a pressure of 5×10^{-7} mbar for a specified time interval. The growth time was calibrated by a break-point analysis and independently by estimation of the Mg flux required to achieve a desired thickness. Rather accurate control of the film thickness can be achieved through variation of the growth time. The cleanliness and composition of the films and underlying crystal were assessed through the use of Auger electron spectroscopy (AES), and further characterization of the electronic structure of the films was achieved through metastable impact electron spectroscopy (MIES) and ultraviolet photoelectron spectroscopy (UPS) (see the Supporting Information).

MIES is a most surface-sensitive technique where the deexcitation of the metastable He* atoms impinging on the surface takes place 3−10 Å above the surface. For oxide materials, the MIES spectra give direct information about the electronic density of states at the surface. The obtained information is similar to that found

from UPS experiments, where the kinetic energy and intensity (flux) of electrons ejected from the target material by incident radiation are measured; in the UPS signal, however, contributions of bulk electronic states overlap with those coming from the surface region. In addition to information obtained from UPS spectra about the electronic density of states, the widths of the UPS spectra yield good estimates of the work functions of the materials being studied.

For all of the defect-poor films investigated in this work, no contributions in the MIES spectra at binding energies between 1 and 3 eV were observed. This is indicative of the absence of FCs on the thin MgO films.[23] The number of FC defects can be varied through variation of the Mg evaporation rate, with shorter evaporation times (i.e., faster evaporation) being associated with films with more defects. Such defect-rich substrates were created by us only for films with larger thicknesses (~10 ML); as aforementioned, the presence of these defects was identified by a MIES signal peaked at ~2 eV (see the Supporting Information).[23]

Clusters of Au_{20} were created through the use of a laser-ablation source[24] using the second harmonic of a 120 Hz Nd:YAG laser. A home-built piezo valve produced a cluster beam from the laser-induced metal plasma using a He carrier gas. The clusters are charge-separated with a quadrupole deflector and subsequently mass-selected using a quadrupole mass spectrometer (ABB-Extrel; mass limit 4000 amu). The clusters were then soft-landed (with an impingement translational energy of 1 eV/cluster) onto the MgO support up to a coverage of 0.3% ML (1 ML = 2.25×10^{15} clusters/cm^2) for temperature-programmed reaction (TPR) studies and 0.5% ML for Fourier transform infrared (FTIR) measurements.

Following preparation of the Au_{20} nanocatalysts, TPR and FTIR studies were performed. For the TPR measurements, ^{13}CO and O_2 were dosed onto the surface (at ~100 K) to an exact coverage using a calibrated molecular beam doser. Exposures of one Langmuir (1 L) O_2 and 1 L ^{13}CO were administered sequentially. Isotope-labeled CO was used to improve the signal-to-noise ratio in the measurements. A temperature-programmed ramp of the catalyst was performed between ~100 and 800 K using a feedback-controlled resistive annealing system of home-built design. Products from the reaction were measured using a quadrupole mass spectrometer. TPR experiments are particularly well suited for the discussion of possible reaction mechanisms because reaction temperatures can be correlated with activation (transition-state, TS) energies obtained from first-principles simulations of the reaction mechanism. These combined experimental and theoretical studies give most valuable information about the reaction mechanism, atomic and molecular arrangements, vibrational frequencies, and electronic structure. Such one-cycle experiments do not give information about catalytic turnover frequencies (TOFs). Determination of the TOF for the catalytic reaction under investigation requires added experiments; indeed, in certain cases, we have applied pulsed molecular beam scattering measurements for this purpose;[25,26] however, in this paper, we do not employ such experiments, focusing on the reaction mechanisms and related atomic and electronic structure factors. Finally, we note that a similar dosing procedure was also carried out for FTIR studies. Following the coadsorption of O_2 and ^{13}CO, FTIR measurements were made at a grazing angle of incidence and the stretching frequencies of ^{13}CO were determined.

b. Theoretical Methods. The first-principles calculations are based on a density functional theory (DFT) approach.[27,28] We

(22) Sterrer, M.; Risse, T.; Heyde, M.; Rust, H. P.; Freund, H. J. *Phys. Rev. Lett.* **2007**, *98*, 032235.

(23) Kalmakov, A.; Stultz, J.; Goodman, D. W. *J. Chem. Phys.* **2000**, *113*, 7564.

(24) Heiz, U.; Vanolli, F.; Trento, L.; Schneider, W. D. *Rev. Sci. Instrum.* **1997**, *68*, 1986.

(25) Röttgen, M. A.; Abbet, S.; Judai, K.; Antonietti, J. M.; Wörz, A. S.; Arenz, M.; Henry, C. R.; Heiz, U. *J. Am. Chem. Soc.* **2007**, *129*, 9635.

(26) Harding, C. J.; Kunz, S.; Habibpour, V.; Teslenko, V.; Arenz, M.; Heiz, U. *J. Catal.* **2008**, *255*, 234.

(27) Kresse, G.; Furtmuller, J. *Phys. Rev. B* **1996**, *54*, 11169.

(28) Kresse, G.; Hafner, J. *Phys. Rev. B* **1993**, *47*, R558.

employed the generalized gradient approximation[29] and ultrasoft pseudopotentials[30] (scalar relativistic ones for gold) with a plane-wave basis (kinetic energy cutoff of 300 eV). We remark here that such calculations have been shown to give very accurate bond lengths (up to 1% too long) and reaction barriers that are accurate to within 25−30% (usually too low) (see p 87 of ref 10). In structural relaxations corresponding to minimization of the total energy, convergence is achieved when the forces on the atoms are less than 0.001 eV/Å. In the following, we describe certain pertinent details of the calculations.

(i) In the calculations for a one-layer-thick MgO film on Mo(100), a (6 × 6) MgO layer containing 36 atoms of Mg and an equal number of O atoms was used, and the underling Mo(100) substrate was modeled by four layers (with a lattice constant of 3.151 Å), each containing 36 Mo atoms. The two bottom layers of the Mo(100) substrate are held static (in the bulk lattice geometry), and in structural optimizations, all of the other atoms of the system (surface atoms, as well as adsorbed cluster and reactant atoms) are allowed to undergo unconstrained relaxation; note that the MgO lattice was stretched in the surface plane by 5% to accommodate the mismatch between the Mo and MgO lattices.

(ii) In calculations involving an eight-layer-thick MgO film on Mo(100), a 5 × 5 periodic cell containing 25 atoms per layer was used. In calculations involving a thick MgO crystal (without a metal support), we used six (6 × 6) MgO layers with one or two oxygen vacancies (FCs) in the top layer; the bottom MgO layer of the slab was kept static with the lattice constant taken as the bulk equilibrium value, 2.998 Å (all other layers, as well as the adsorbed gold nanocluster and the reactants, were allowed to relax dynamically).

Finally, we note that the large size of the computational supercell used by us [up to (6 × 6) larger than the planar unit cell of the MgO(100) and Mo(100) substrate, i.e., equivalent to a 6 × 6 k-point sampling when a single planar unit cell is used for the substrate] justifies the $k = 0$ (Γ-point sampling) calculations that we employed here. Comparisons between the $k = 0$ calculations and test computations that included explicit k-point sampling (2 × 2 × 1 and 4 × 4 × 1, i.e., increasing the effective number of k points up to 24 × 24 × 1) provided clear evidence that the $k = 0$ results are indeed well converged, with differences in the total energies well below 1% and differences (in comparison with the $k = 0$ results) of at most 1% between the binding energies. We conclude that added k-point sampling has no discernible effect on the results of our computations.

Results and Discussion

a. Experimental Findings. The isotopically labeled product signals of the TPR experiments are shown in Figure 1, where variation of the reactivity with the MgO film thickness is illustrated for films containing no FC defects (labeled as defect-poor films). In a first experiment, Au_{20} clusters were deposited on a Mo support, which was exposed to oxygen at the same conditions as those in a typical MgO film preparation step (5 × 10^{-7} mbar of O_2, $T = 300$ K, 20 min). The electronic structure of this surface was characterized by MIES and UPS and indicates the presence of a partially oxidized Mo surface (see the Supporting Information). This experiment is rather important because thin MgO films of thicknesses of up to about 3 ML are not necessarily continuous, and consequently Au_{20} clusters deposited between MgO islands could be assumed (erroneously as we discuss below) to contribute to the formation of CO_2 in addition to the reaction catalyzed by the gold clusters anchored on the MgO film. That the interisland (oxidized Mo) surface regions do not contribute to the CO oxidation reaction has been
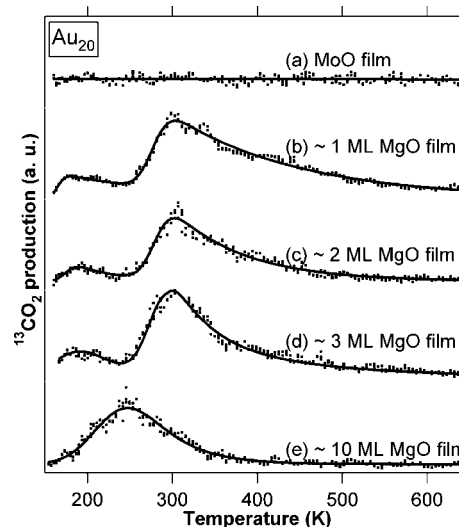

Figure 1. TPR spectra illustrating $^{13}CO_2$ formation produced using a nanocatalyst based on Au_{20} clusters at a coverage of 0.3% ML deposited onto MgO films of various thickness (1−10 ML). Markers represent the experimental data points; the solid line is a multipeak exponential Gaussian fit drawn to guide the eye.

verified by TPR measurements on Au_{20} deposited on partially oxidized Mo surfaces, where no $^{13}CO_2$ signal (the product of the oxidation reaction) has been recorded. On the other hand, when MgO films grown on the Mo(100) surface are used as supports for the gold clusters, the oxidation reaction is found to occur for various MgO coverages, corresponding to different film thicknesses (Figure 1b−d). In these experiments, the MgO film is grown so that the coverage is 3 ML or less. However, as indicated above, it is not assumed that at a film thickness of 1−3 ML the film is continuous; in fact, MgO films on Mo are known to grow via island formation. It is therefore likely that, although a film is calculated to have 1−3 ML coverage, the film actually consists of islands that are one to three layers thick, interspaced by partially oxidized Mo. Because, as aforementioned, gold clusters deposited on partially oxidized Mo are not reactive, we conclude that only Au_{20} clusters on MgO islands contribute to the observed catalytic activity.

On relatively thin MgO films (<3 ML), the observed TPR shows two regimes of CO_2 formation: a minor peak at ∼180 K with the major product formation occurring at ∼300 K. The reactivity associated with the nanocatalyst varies as the film thickness is increased. From TPR studies made on thick MgO films (∼10 ML), which are found from break-point analysis to be continuous, we observe that the reactivity of the gold catalyst on such films is notably different compared to that of the thinner MgO film case. In particular, the TPR records for the thicker films exhibit a single peak at ∼250 K, which is markedly lower than the higher temperature peak for the aforementioned thin-film-based nanocatalysts.

To explore the effects of film composition on the reactivity, measurements were performed on defect-rich and defect-poor thick films (Figure 2). Unlike the low-temperature reactivity of the defect-poor thick films (Figure 2a), which exhibits a single reaction channel, TPR studies on defect-rich films (Figure 2c) show two reaction regimes. The lower temperature reactivity is observed at ∼200 K, and the higher temperature reactive regime is located in the vicinity of 400 K.

Further investigations of the effects of defects on the Au_{20} catalytic activity employed FTIR spectroscopy. Low-temperature

(29) Perdew, J. P.; Chevary, J. A.; Vosko, S. H.; Jackson, K. A.; Pederson, M. R.; Singh, D. J.; Fiolhais, C. *Phys. Rev. B* **1992**, *46*, 6671.

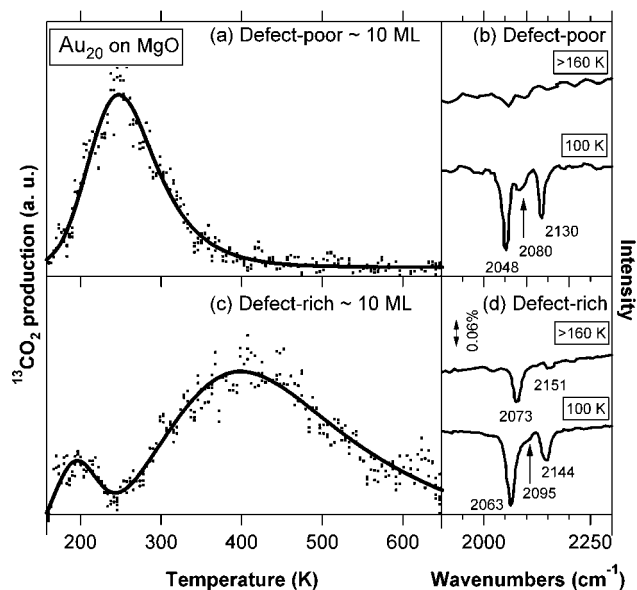(30) Vanderbilt, D. *Phys. Rev. B* **1990**, *41*, 7892.

Figure 2. (a) TPR measurements made on Au_{20}-based nanocatalysts using thick, defect-poor MgO films (~10 ML). Markers show the experimental data points, and the line is a multipeak exponential Gaussian fit to the data. (c) TPR measurements made on Au_{20}-based nanocatalysts using thick, defect-rich MgO films. Markers show the experimental data points, and the line is a multipeak exponential Gaussian fit to the data. Parts b and d are FTIR studies corresponding to parts a and c, respectively. All measurements are made with a 0.5% ML coverage of Au_{20}.

stretching frequencies of ^{13}CO coadsorbed with $^{18}O_2$ are shown in parts b and d of Figure 2. At low temperature (100 K) and prior to CO combustion, Au_{20} on both defect-poor and -rich MgO films readily adsorbs ^{13}CO. Three bands at 2048, 2080, and 2130 cm^{-1} are observed for the model catalysts with defect-poor support materials. Note that ^{13}CO on MgO reveals a typical band at 2127 cm^{-1} but with less intensity than is observed in the spectrum shown in Figure 2b. On defect-rich support materials, Au_{20} adsorbs ^{13}CO with vibrational frequencies at 2063, 2095 (observed as a small shoulder), and 2144 cm^{-1}. After initiation of the reaction at temperatures larger than 160 K, CO desorbs almost totally or reacts to completion on Au_{20} supported on defect-poor films, whereas for Au_{20} supported on defect-rich films, CO remains adsorbed at these temperatures. This observation is in concert with the low-temperature catalysis of the CO oxidation reaction, observed for Au_{20} clusters supported on defect-poor films. Interestingly, the shift of the main band observed for CO adsorbed on Au_{20} on defect-poor and -rich films is only 15 cm^{-1} in comparison to 53 cm^{-1} in the case of Au_8 adsorbed on identical films.[14]

b. Cluster Structures, Electron Charge Distributions, and Binding Energies. To elucidate the microscopic mechanisms that underlie the above observations pertaining to the catalytic activity of surface-supported Au_{20} clusters, we have performed first-principles DFT electronic structure calculations, coupled with atomic structural optimizations and simulations of the reaction pathways, for Au_{20} adsorbed on MgO surfaces. While for the thicker MgO films the tetrahedral [i.e., $Au_{20}(T)$] structure of the cluster is by far the most stable one, on thin MgO films supported on Mo(100), a "wetting" planar (quasi-2D) island configuration [$Au_{20}(P)$] is energetically favorable because of an increased number of contacts with the substrate, leading to a larger accumulation of interfacial charge (originating from the underlying Mo substrate); as noted previously,[3] the attraction between the interfacial excess electronic charge and its image

in the underlying material substrate is the source of the stabilization of the planar geometry of the deposited gold cluster. However, because in the gas phase the deposited Au_{20} clusters have a tetrahedral three-dimensional (3D) structure, it is likely that not all of the clusters on the thin MgO(100)/Mo film have attained the optimal 2D structure after deposition. Consequently, for the thin MgO films, we consider reactions catalyzed either by the 2D $Au_{20}(P)$ adsorbed cluster (Figure 3a) or by the 3D $Au_{20}(T)$ isomer (Figure 3b), which are likely to coexist on the surface. Similarly, for the case of a thick MgO(100) crystal containing oxygen vacancies (for TPR experiments, see Figure 2c), we consider two possible isomers of the Au_{20} cluster. One of these isomers is the tetrahedral $Au_{20}(T)$ adsorbed on top of an oxygen vacancy located near the middle of the base facet of the tetrahedron in Figure 3c. The other isomers that we consider are (i) a bilayer cluster, Au_{20}(bilayer; FC), adsorbed on an oxygen vacancy located near the middle of the bottom facet (see Figure 3d) and (ii) a bilayer cluster, Au_{20}(bilayer; 2FC), adsorbed on top of two neighboring FCs located near the middle of the bottom facet (see Figure 3e). In all of these configurations, the oxygen vacancies located under the adsorbed gold nanocluster are stable against annealing (for example, by one of the O atoms of the reactant molecule).

The optimal structures of the 2D and 3D isomers together with isosurfaces of the excess electron charge distribution, Δq, which is seen to be accumulated mainly in the interface of the cluster with the MgO(1 L)/Mo(100) surface, are shown in parts a and b of Figure 3, respectively. The binding energy of $Au_{20}(P)$ (Figure 3a) to the surface is $E_B = 12.50$ eV with $\Delta q = 1.62$ e, while $Au_{20}(T)$ (Figure 3b) is anchored less strongly, with $E_B = 5.73$ eV and $\Delta q = 1.06$ e; the relaxed structure of $Au_{20}(T)$ adsorbed on an eight-layer-thick MgO film supported on Mo(100) was found to be similar to that shown in Figure 3b, with $E_B = 3.00$ eV and $\Delta q = 0.73$ e.

In Figure 3c−e, we show ground and higher energy isomeric structures of Au_{20} clusters adsorbed on the (100) surface of a thick MgO crystal (with no metal support) with oxygen vacancies, as described above. The binding energies of the clusters $Au_{20}(T)$ in part c and Au_{20}(bilayer) in parts d and e are 4.36 eV (for part c), 4.92 eV (for part d), and 7.93 eV (for the 2FC case displayed in part e). In the gas phase, the tetrahedral cluster is more stable than the bilayer one by 1.57 eV.

Superimposed on the atomic structures in Figure 3c−e, we display the excess electron densities, which show charge accumulation in the interfacial region between the cluster and the surface; this excess charge originates mainly from the FC defects in the MgO surface. In addition, we show for the $Au_{20}(T)$ cluster adsorbed on the single FC the electronic charge distribution corresponding to the highest occupied Kohn−Sham (HOKS) orbital, which is seen to exhibit maxima at the top (apex) atom of the tetrahedron, as well as at the interfacial region in the vicinity of the FC (see the right frame in Figure 3c); adsorption of an O_2 molecule is likely to occur in those regions, where the density of the electrons in the HOKS orbital is higher (see below).

c. Reaction Mechanisms of CO Combustion on Supported Au_{20} Clusters. In this section, we explore several reaction mechanisms corresponding to the various model catalyst systems investigated in the TPR experiments (Figures 1 and 2). The reaction profiles (pathways) that we present were obtained via first-principles quantum calculations (see the Theoretical Methods section). In these calculations, a reaction coordinate was judiciously chosen (that is, the distance between two reacting
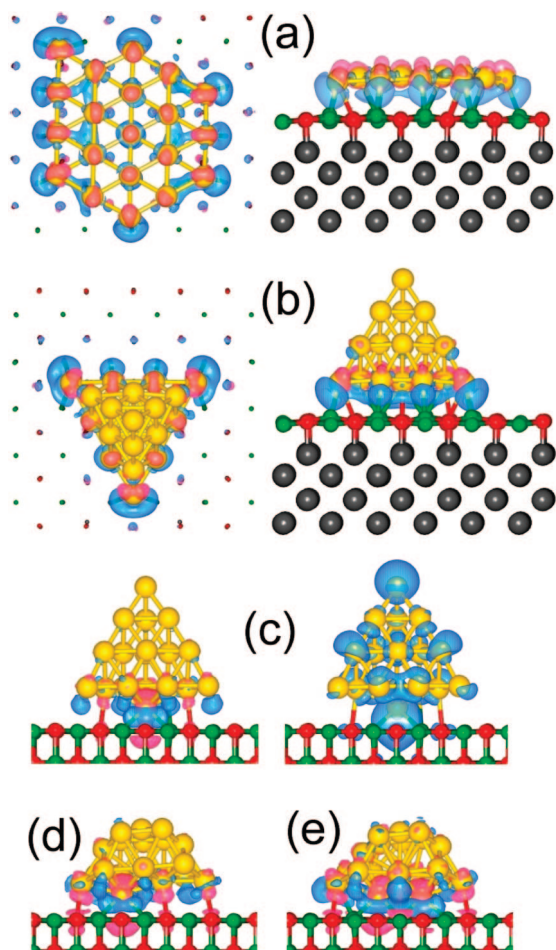
Figure 3. Minimum-energy structures of Au_{20} clusters adsorbed on surfaces. (a) Top (left) and side (right) views of a planar gold cluster adsorbed on a one-layer-thick MgO layer, supported on Mo(100), $Au_{20}(P)/MgO(1\ L)/Mo$. (b) Same as in that in part a for a 3D tetrahedral gold cluster. The binding energies of the clusters (with reference to the separated gas-phase clusters and surface subsystems) are 12.50 eV for the planar cluster (a) and 5.73 eV for the 3D one (b). Superimposed on the atomic structures are density isosurfaces corresponding to the excess electronic charge distributions (blue corresponds to charge accumulation and pink signifies charge depletion with reference to the isolated cluster and surface components); these excess electron distributions are obtained from the difference between the charge distribution of the combined system [i.e., gold cluster adsorbed on the MgO surface, with or without a Mo(100) support] and the charge distributions of the isolated components (in the optimal geometry determined for the combined system), that is, (i) the Au_{20} gold cluster and (ii) the MgO surface [with or without a Mo(100) support]. Note the charge accumulation at the interfacial periphery regions. (c) Left: Excess electronic charge distribution for a tetrahedral Au_{20} cluster adsorbed on an FC (on the surface of a thick MgO film), located under the middle of the bottom facet of the cluster. Right: Electron density isosurface of the HOKS orbital, showing charge accumulation about the top apex atom, as well as near the oxygen vacancy; the isosurface encompasses 61% of the electron density in the doubly occupied orbital (i.e., 1.23 e). (d) Bilayer isomer of Au_{20} with a surface FC located near the middle of the bottom facet of the adsorbed cluster. (e) Bilayer cluster with a dimer of neighboring FCs located near the middle of the bottom fact of the adsorbed cluster. The binding energies of the clusters to the MgO surface [with reference to the energy of the isolated systems, MgO surface, and the corresponding gas-phase cluster, i.e., $Au_{20}(T)$ in part c and Au_{20}(bilayer) in parts d and e] are 4.36 eV (for part c), 4.92 eV (for part d), and 7.93 eV (for the 2FC case displayed in part e). In the gas phase, the tetrahedral cluster is more stable than the bilayer one by 1.57 eV. Superimposed in parts c and d are equidensity surfaces of the excess electron charge density, with blue and pink corresponding to charge excess and charge depletion, respectively. The excess electronic charges are (c) $\Delta q[Au_{20}(T;\ FC)] = 1.80$ e, (d) $\Delta q[Au_{20}$(bilayer; FC)] = 2.10 e for the bilayer isomer in part d, and (e) $\Delta q[Au_{20}$(bilayer; 2FC)] = 2.85 e. Color designation: Au atoms in yellow, O atoms in red, Mg atoms in green, and Mo atoms in black.

atoms, for example, the distance between the C atom of an adsorbed CO molecule and the nearest O atoms of an adsorbed O_2 molecule), and the total energy of the system was optimized for given values of the reaction coordinate, through unconstrained relaxation of all of the other degrees of freedom of the system (reactant molecules, gold cluster atoms, MgO surface atoms, and those of the underlying Mo substrate). The reaction profiles were obtained via repeating such calculations for various values of the chosen reaction coordinate. These calculations yield results that are the same as, or close to, those obtained by other methods [e.g., the nudged elastic band and variants thereof (see the discussion on pp 89 and 90 in ref 10)]. Finally, we note that while in the following we give calculated reaction barriers with an accuracy of two decimal figures (e.g., 0.34 eV), rounding off to one decimal figure (i.e., 0.3 eV) is appropriate.

i. Low-Temperature Mechanisms of Au_{20} Adsorbed on Thin MgO Films. We model the thin MgO films used in the measurements (Figure 2b–d, with MgO coverage up to 1 ML) by an extended monolayer thin MgO film adsorbed on Mo(100). We have found in previous studies that the reactivity of metal-supported MgO films remains similar for film thicknesses of up to three layers.[4] Furthermore, we choose to focus on systematic trends correlated with the thickness of the MgO support and not to consider adsorption of gold clusters onto MgO islands (e.g., adsorption at island step interfaces with the underlying molybdenum oxide) because gold clusters adsorbed on molybdenum oxide (between the MgO islands) are catalytically nonactive; the properties of gold clusters adsorbed on the top facet of such MgO islands are similar to those adsorbed on the extended MgO films. In addition, we focus only on MgO films adsorbed on Mo(100); i.e., we do not model MgO layers adsorbed on molybdenum oxide (which may also be generated during the growth process); our demonstrated ability to successfully describe the experimentally observed trends (see below) supports a posteriori our model assumptions.

As depicted in Figure 1b–d, Au_{20} deposited on thin MgO films forms CO_2 at temperatures below 200 K in a one-heating-cycle experiment. To model possible reaction mechanisms, we consider the reactivity of thin film (one-layer MgO) $Au_{20}/MgO(1\ L)/Mo$ systems. Molecular oxygen adsorbs at the interface between the $Au_{20}(P)$ cluster and the MgO surface with a binding energy, $E_B[O_2/Au_{20}(P)]$, of 3.06 eV; the adsorbed molecule is activated to a peroxo state [$d(O-O) = 1.515$ Å] via occupation of the antibonding $2\pi^*$ orbital (see leftmost configuration in Figure 4a). Clearly, oxygen adsorbs at the location of highest charge accumulation. Through TS simulations (consisting, as described above, of ground-state electronic structure calculations and structural relaxations for adiabatically slow variation of the reaction coordinate, i.e., the O–O bond in this case), we determined a dissociation barrier of 0.34 eV with $d_{TS}(O-O) = 1.95$ Å (Figure 4a). Relaxation from the TS configuration results in the (rightmost) configuration displayed in Figure 4a, with $d(O-O) = 3.29$ Å. The reaction between this dissociated configuration of the adsorbed O_2 molecule and a CO molecule adsorbed on top of a surface Mg atom [with a binding energy of 0.47 eV and $d(CO) = 1.14$ Å] at a distance $d[C-O(1)] = 3.10$ Å between the C atom and the closest O atom of the adsorbed O_2 molecule [denoted here and in the following as O(1)] is shown in Figure 4c. In this reaction, formation of an adsorbed CO_2 intermediate (TS configuration in Figure 4c, with $d[C-O(1)] = 1.80$ Å, $d(C-O) = 1.17$ Å, and $d[O-O(1)] = 3.285$ Å) involves an essentially negligible barrier (0.07 eV), and the desorption energy of the CO_2 product (from the leftmost
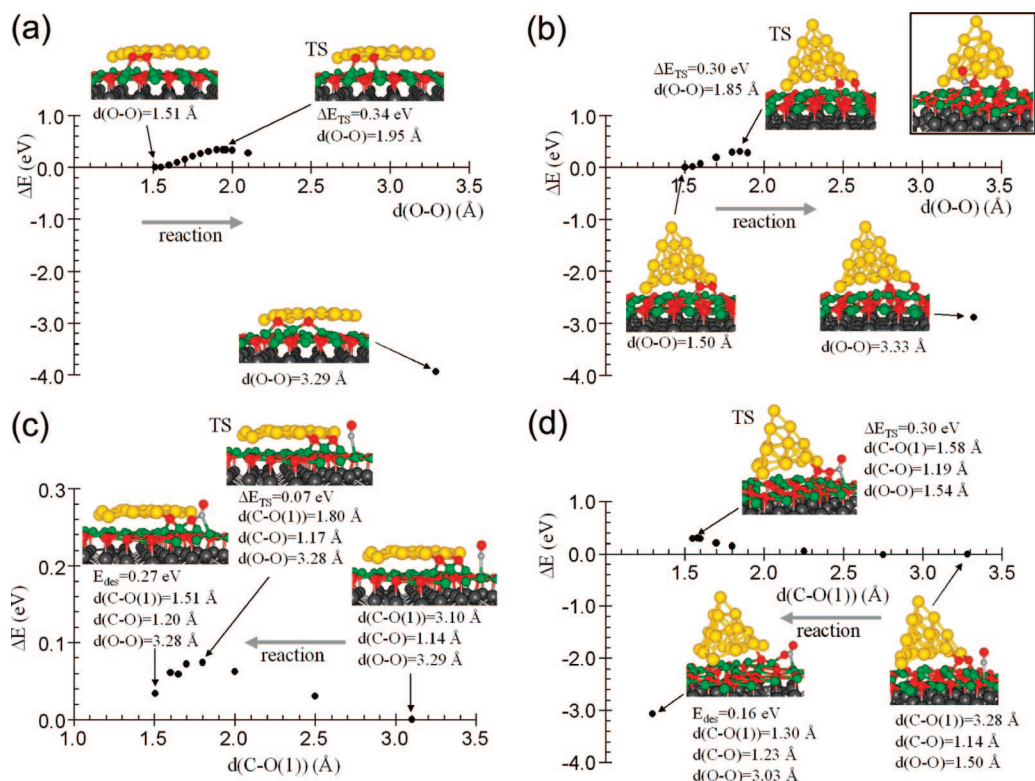
Figure 4. (a and b) Reaction paths for the dissociation of O_2 on 2D and 3D (tetrahedral) Au_{20} adsorbed on a one-layer thin MgO film supported on Mo(100). In both cases, the TS activation energy is relatively low: $\Delta E_{TS} = 0.34$ eV for the 2D gold structure (a) and $\Delta E_{TS} = 0.30$ eV for the 3D adsorbed cluster (b). In the inset to frame b, we show the relaxed structure of the adsorbed CO_2 molecule produced by the reaction of the dissociated O_2 molecule on $Au_{20}(T)$/MgO(1 L)/Mo with CO; no energy barrier is involved in this reaction, which starts from the dissociated O_2 molecule and a CO adsorbed on the MgO surface (on top of a Mg atom, with an adsorption energy of 0.55 eV), at a distance of 2.48 Å between the C atom and the closest dissociated O atom. The desorption energy of the product CO_2 is 0.31 eV. This reaction contributes to the low-temperature peak shown in Figure 1b–d. In parts c and d, we display two other low-temperature reactions pathways. The reaction in part c corresponds to an adsorbed planar, $Au_{20}(P)$ cluster, and it starts from the adsorbed dissociated O_2 molecule shown in part a (with a dissociation activation energy of 0.34 eV) and a CO molecule adsorbed on top of a Mg atom [$E_B(CO) = 0.47$ eV]. The generation of adsorbed CO_2 entails a TS barrier of $E_{TS} = 0.07$ eV and a desorption energy of the product $E_{des}(CO_2) = 0.27$ eV. The reaction in part d corresponds to an adsorbed 3D $Au_{20}(T)$ cluster, and it involves a peripherally adsorbed activated O_2 molecule and a CO molecule adsorbed on the MgO surface ($E_B = 0.41$ eV). The reaction in part d entails a TS barrier $\Delta E_{TS} = 0.30$ eV, and the desorption energy of the product is $E_{des}(CO_2) = 0.16$ eV. Color designation (online): Mg atoms in green, O atoms in red, Au atoms in yellow, C atoms in light gray, and Mo atoms in dark gray.

configuration in Figure 4c) is $E_{des} = 0.27$ eV. The bottleneck for this reaction consists of overcoming the relatively low dissociation barrier (Figure 1a), and thus this reaction channel contributes to the observed low-T reactivity on the thin MgO film (Figure 1b–d).

Other reaction channels that may contribute to the low-temperature reactivity are shown in parts b and d of Figure 4, with both involving 3D $Au_{20}(T)$/MgO(1 L)/Mo model catalysts. The reaction in Figure 4b again involves dissociative adsorption of O_2 at the interfacial cluster periphery [with a TS barrier of 0.30 eV and $d_{TS}(O-O) = 1.85$ Å]. Relaxation from the TS configuration results in the (rightmost) structure shown in Figure 4b, with $d(O-O) = 3.33$ Å. The reaction of the O(1) atom of the dissociated O_2 molecule with a CO molecule adsorbed with a binding energy of 0.55 eV on the MgO surface is essentially barrierless. Relaxation of the TS complex yields an adsorbed CO_2 intermediate (see inset in Figure 4b, with $d[C-O(1)] = 1.52$ Å, $d(C-O) = 1.20$ Å, and $d[O-O(1)] = 3.41$ Å), whose desorption energy is $E_{des} = 0.31$ eV. The other low-temperature channel, shown in Figure 4d, does not involve dissociation of the adsorbed O_2 molecule. Instead, it starts from an interfacial-periphery adsorbed O_2 molecule that is activated to a peroxo state [$d(O-O) = 1.504$ Å] and a CO molecule adsorbed on the MgO surface with a binding energy of 0.41 eV. Formation of CO_2 entails a TS barrier of 0.3 eV (occurring at $d_{TS}[C-O(1)]$

$= 1.58$ Å and $d_{TS}(O-O) = 1.54$ Å), with subsequent relaxation yielding an adsorbed CO_2 intermediate ($d[C-O(1)] = 1.30$ Å, $d(C-O) = 1.23$ Å) and an essentially dissociated O_2 molecule ($d[O-O(1)] = 3.03$ Å); the desorption energy to form gaseous CO_2 is 0.16 eV. We note that here, as well as in the other low-temperature reaction channels discussed above, diffusion of the reactant CO on the MgO film to the proximity of the adsorbed cluster is assumed.[31,32]

ii. High-Temperature Mechanisms on Au_{20} Adsorbed on Thin MgO Films. The main contribution of the CO_2 signal in the TPR experiments (Figure 1b–d) is observed at around 300 K. While, as described above, for the 2D $Au_{20}(P)$/MgO(1 L)/Mo catalyst reaction of adsorbed CO with predissociated peripherally adsorbed O_2 leads to a low-temperature reaction, when the surface-adsorbed CO reacts with an activated, but undissociated peripherally adsorbed O_2, a relatively high TS reaction barrier of 0.66 eV is found (Figure 5a, with $d_{TS}[C-O(1)] = 1.54$ Å and $d_{TS}(C-O) = 1.20$ Å). Subsequent desorption of the adsorbed CO_2 intermediate involves a desorption energy $E_{des} = 0.29$ eV. We note that for this case we considered the initial surface adsorption of two CO molecules

(31) Harding, C. J.; Kunz, S.; Habibpour, V.; Heiz, U. *Chem. Phys. Lett.* **2008**, *461*, 235.

(32) Harding, C. J.; Kunz, S.; Habibpour, V.; Heiz, U. *Phys. Chem. Chem. Phys.* **2008**, *38*, 5875.
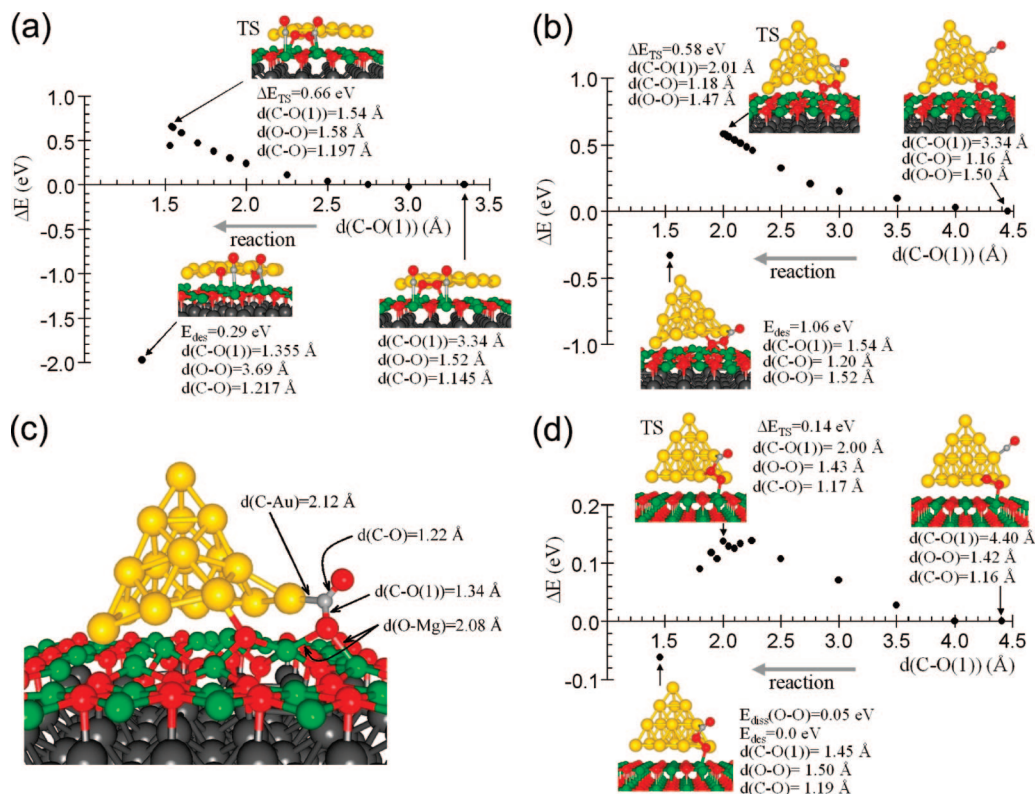
Figure 5. (a−c) High-temperature pathways of CO with O_2 catalyzed by for Au_{20} adsorbed on MgO(1 L)/Mo(100). (a) Formation of CO_2 through the reaction of a CO molecule adsorbed on the MgO surface with $E_B(CO) = 0.44$ eV, near an activated O_2 molecule adsorbed at the interfacial periphery of a planar (2D) $Au_{20}(P)$ cluster on the 1 L MgO film with $E_B(O_2) = 3.06$ eV and $d(O-O) = 1.52$ Å. The reaction entails a TS energy barrier of 0.66 eV, and the desorption of the CO_2 product requires $E_{des} = 0.29$ eV. The reaction of the second adsorbed CO with the remaining O atom proceeds with no activation barrier; however, the desorption of the resulting adsorbed CO_2 molecule requires an energy of 0.60 eV. (b) Pathway of the oxidation reaction catalyzed by a tetrahedral 3D $Au_{20}(T)$ cluster, with an activated O_2 molecule adsorbed at the peripheral interface of the cluster with the underlying 1 L MgO film [$E_B(O_2)$ = 4.19 eV] and a CO molecule adsorbed on the gold cluster [$E_B(CO) = 0.6$ eV]. The TS barrier for the reaction is 0.58 eV, and desorption of the product CO_2 molecule requires 1.06 eV. (c) Enlarged view of the desorbing CO_2 molecule, showing a configuration with the C atom bonded to the gold cluster and one of the O atoms bonded to two Mg surface sites [$d(O-O) = 2.08$ Å], resulting in a relatively high desorption energy. (d) CO combustion reaction pathway catalyzed by a tetrahedral $Au_{20}(T)$ cluster adsorbed on an eight-layer-thick MgO film supported on Mo(100) (see Figure 2a). In the initial configuration, an activated O_2 molecule is adsorbed [$E_B(O_2) = 0.65$ eV] at the cluster interface with the magnesia film and a CO molecule is bonded to a second-layer Au atom of the cluster [$E_B(CO) = 0.50$ eV]. The formation of a CO_2 product entails a 0.14 eV TS barrier, and the molecule desorbs readily. Color designation (online): Mg atoms in green, O atoms in red, Au atoms in yellow, C atoms in light gray, and Mo atoms in dark gray.

proximal to the gold cluster (with a binding energy of 0.44 eV per molecule; see Figure 5a). Formation of a second adsorbed CO_2 molecule via reaction of the second CO with the remaining O atom adsorbed at the gold cluster periphery was found to occur with essentially no activation barrier, but the formation of gaseous CO_2 entails a relatively high desorption energy E_{des} = 0.60 eV; note that one of the O atoms of the adsorbed CO_2 molecule is bonded also to a Mg atom of the magnesia surface, which accounts for the somewhat elevated desorption energy of the product molecule. We conclude that the reactions of both O atoms with surface-adsorbed CO are predicted to contribute to the higher temperature channel observed experimentally.

Another reaction channel that involves a relatively high activation barrier was found for the system $CO/O_2/Au_{20}(T)/$ MgO(1 L)/Mo (see Figure 5b), where an O_2 molecule is bound to the periphery of the cluster (where the excess charge accumulation is highest) with a binding energy $E_B(O_2)$ of 4.19 eV. The O_2 molecule is peroxo-activated [$d(O-O) = 1.50$ Å] and interacts with an adsorbed CO bonded to the second layer of the 3D gold cluster with E_B of 0.6 eV. Note that also at this location a slight charge accumulation is calculated (see Figure 3b). The TS barrier is 0.58 eV, and the corresponding TS depicted in Figure 5b is characterized by a $d_{TS}[C-O(1)]$ of 2.01 Å, a $d_{TS}(C-O)$ of 1.18 Å, and a $d[O-O(1)]$ of 1.47 Å. An

upper bound estimate of the desorption energy required for the formation of a gaseous CO_2 product is $E_{des} = 1.06$ eV; this rather high calculated desorption energy is attributed to the strong bonding of one of the O atoms of the adsorbed product CO_2 molecule to the magnesia surface, with the formation of bonds to two Mg sites of the monolayer MgO film (see Figure 5c), enhanced by the excess accumulation of electronic charge originating from the underlying metal [Mo(100)] support.

iii. Reaction Mechanisms of Au_{20} Adsorbed on Thick, Defect-Free MgO Films. To explore the mechanisms underlying the relatively low-temperature reactivity peak at $T \approx 250$ K, observed on defect-poor thicker (8−10 ML) films (Figure 2a), we considered a defectless eight-layer-thick MgO film, i.e., the model catalyst $Au_{20}(T)/MgO(8 L)/Mo$ (see Figure 5d). We start from an equilibrated configuration of peripherally adsorbed O_2 [$E_B(O_2) = 0.65$ eV in a peroxo-activated state and $d(O-O) =$ 1.41 Å] and a CO molecule bonded [$E_B (CO) = 0.50$ eV] to a Au atom in the second layer of the gold cluster. The formation of a TS (Figure 5d) occurs with a low barrier of 0.14 eV at $d[C-(O(1)]$ of 2.0 Å, and the desorption of CO_2 involves a very small exit barrier. Note the drastic decrease in the reaction and exit barriers when compared to $Au_{20}(T)/MgO(1 ML)Mo$ (see Figure 5b), that is, from $\Delta E_{TS} = 0.58$ eV and $E_{des} = 1.06$ eV for the thin MgO film to $\Delta E_{TS} = 0.14$ eV and $E_{des} = 0$ for

the thicker one. This illustrates the marked influence of the underlying metal surface on the catalytic activity of the adsorbed $Au_{20}(T)$ cluster. In particular, the thin MgO layer allows for enhanced charge accumulation [originating from the underlying Mo(100) substrate], which serves to enhance the activation of adsorbed species (specifically O_2). However, the electronic charge transferred through the thin metal oxide film enhances binding of intermediates and reaction products to the surface, and consequently, in certain cases, one finds for this system higher activation barriers for exit channels corresponding to dissociation of (TS and post-TS) intermediate reaction complexes or desorption of the product molecule (e.g., CO_2).

iv. Reaction Mechanisms on Au_{20} Adsorbed on Defective Thick MgO Films. In all of the cases discussed above, the MgO films were defectless, and the catalytic activity was enabled by the excess electronic charge (originating from the underlying metal [Mo(100)] support) accumulated at the interface of the gold nanocluster with the magnesia film. We turn now to analysis of the experiments performed on a defect-rich thick MgO(100) surface, where any effects due to an underlying metal support are absent. In the data shown for this system in Figure 2c, the broad distribution of the reactivity (the smaller peak at ~210 K and the main broad distribution peaking at ~400 K) can be correlated with the multiplicity of adsorbed cluster configurations that may coexist on such surfaces. These competing configurations differ from each other by the isomeric structure of the adsorbed nanocluster and the nature of the binding of the cluster to the surface; in particular, we consider anchoring of clusters to single or double (nearest-neighbor) surface oxygen vacancy (FC) defects (see Figure 3c−e). First we considered a single FC defect located under the middle of the bottom facet of the adsorbed tetrahedral Au_{20} cluster [$Au_{20}(T)/MgO(FC)$], whose binding energy to the MgO surface is 4.36 eV. An O_2 molecule adsorbs to the top apex Au atom of the $Au_{20}(T)$ cluster with a binding energy $E_B(O_2) = 0.28$ eV and a bond distance $d(O-O) = 1.28$ Å (see Figure 6a); we recall here that for this system the HOKS orbital exhibited electronic charge accumulation at the apex atom (see the right frame in Figure 3c), where the O_2 molecule adsorbs. It reacts with adsorbed CO [$E_B(CO) = 0.54$ eV], reaching a relatively low TS barrier of 0.41 eV at $d_{TS}[C-O(1)] = 1.75$ Å, $d_{TS}(C-O) = 1.18$ Å, and $d_{TS}[O-O(1)] = 1.35$ Å (see Figure 6a) and resulting in a post-TS $CO-O_2$ complex (see the leftmost configuration in Figure 6a). Dissociation of the complex requires an energy $E_{diss} = 0.49$ eV, and desorption of the product CO_2 molecule occurs with no exit barrier.

Other initial adsorption configurations that we have explored include peripherally adsorbed O_2 with CO adsorbed either on the MgO surface or on the tetrahedral cluster. In all of these cases, we obtained activation barriers in the range of 0.6−0.75 eV. For example, starting from a peripheral adsorption of O_2 [$E_B(O_2) = 0.49$ eV] yielding a peroxo-activated molecule [$d(O-O) = 1.49$ Å] and a CO molecule adsorbed on the MgO surface ($E_B(CO) = 0.28$ eV, $d[C-O(1)] = 3.02$ Å, $d(C-O) = 1.14$ Å) resulted in a TS barrier $\Delta E_{TS} = 0.62$ eV, with $d_{TS}[C-O(1)] = 1.65$ Å, $d_{TS}(C-O) = 1.18$ Å, and $d_{TS}(O-O) = 1.56$ Å, which relaxes to a state with an adsorbed CO_2 molecule ($d[C-O(1)] = 1.18$ Å, $d(C-O) = 1.17$ Å, and $d(O-O) = 3.20$ Å). Desorption of the product CO_2 molecule is found to involve a negligible barrier.

Next we consider several reaction pathways involving a bilayer isomeric form of the adsorbed Au_{20} cluster (see Figure 3d,e):

(A) First we display in Figure 6b the pathway for the reaction on a bilayer isomer anchored on a single FC defect (the binding energy of the cluster to the surface is calculated to be 4.92 eV). Here the reaction starts from a peripherally adsorbed O_2 molecule [$E_B(O_2) = 0.63$ eV], which is activated to a peroxo state [$d(O-O) = 1.43$ Å] and a surface-adsorbed CO molecule [$E_B(CO) = 0.29$ eV] with the distance between the C atom to the nearest O atom of the O_2 molecule $d[C-O(1)] = 2.48$ Å. The TS barrier for the formation of an adsorbed $CO-O_2$ complex (characterized by $d_{TS}[C-O(1)] = 1.60$ Å, $d_{TS}(C-O) = 1.20$ Å, and $d_{TS}[O-O(1)] = 1.49$ Å) is 0.29 eV, and dissociation of the interoxygen bond between the complex and the other oxygen of the reactant O_2 molecule entails an activation energy $E_{diss}(O-O) = 0.43$ eV. Desorption of the product CO_2 molecule from the surface is barrierless.

(B) A somewhat higher temperature reaction pathway is shown in Figure 6c for a reaction catalyzed by a bilayer cluster adsorbed on top of two neighboring oxygen vacancies, both located in the vicinity of the middle of the bottom facet of the cluster. The binding energy of this isomer to the surface is $E_B[Au_{20}(bilayer)] = 7.93$ eV (see Figure 3e). The reaction starts from a peripherally adsorbed [$E_B(O_2) = 0.84$ eV], peroxo-activated [$d(O-O) = 1.51$ Å] O_2 molecule and a CO molecule adsorbed on the bilayer gold cluster [$E_B(CO) = 0.81$ eV]. The barrier for formation of a TS $CO-O_2$ complex is 0.26 eV, and the dissociation process of the complex (see above) entails an energy $E_{diss} = 0.51$ eV. Desorption of the product CO_2 molecule is found to be barrierless.

We digress here to illustrate one of the key principles of nanocatalysis, namely, "dynamical structural fluctionality",[18] which expresses the ability of the catalytic center (here the surface-supported gold nanocluster) to change its atomic structure (atomic arrangement) in the course of the reaction. This property is illustrated by following, in the course of the oxidation reaction, the relative positions of the three Au atoms marked (by numbers 1, 2, and 3) in the inset to Figure 6c. In the initial state (minimum-energy configuration) of the adsorbed reactants (the rightmost structure in Figure 6c), the angle formed by the three marked Au atoms (with the atom marked 2 being at the apex of the triangle) takes the value $\theta(123) = 59°$. As the TS is approached (decreasing the distance $d[C-O(1)]$ between the C atom and the closest O atom of the adsorbed O_2 molecule), the above angle increases to a value of $\theta_{TS}(123) = 76°$. The relaxed configuration (the leftmost structure in Figure 6c) is characterized by $\theta(123) = 79°$. We note here that the fluctional structural distortions of the metal cluster, illustrated above, occur to various degrees in all of the reactions described in this study, with the largest structural distortions observed when both reactants adsorb on the metal cluster. These structural variations serve to enhance the adsorption of the reactants and to lower the activation barriers for reactions between the adsorbed reactants. We note here that the activation of the reactant O_2 molecule (to form a superoxo- or peroxo-like state through occupation of the antibonding orbital, as discussed above), which is manifested by elongation of the O−O bond of the adsorbed molecule (located often at the cluster peripheral interface with the underlying MgO surface) by up to $\Delta d(O-O) = 0.25$ Å, is accompanied by changes in the positions (relative distances) of the Au atoms in the vicinity of the adsorption site.

(C) As an example of a higher temperature reaction, we show in Figure 6d the pathway of a reaction catalyzed by the bilayer gold cluster adsorbed on a single surface FC (as in Figure 6b), starting from a peripherally adsorbed, peroxo-activated, O_2
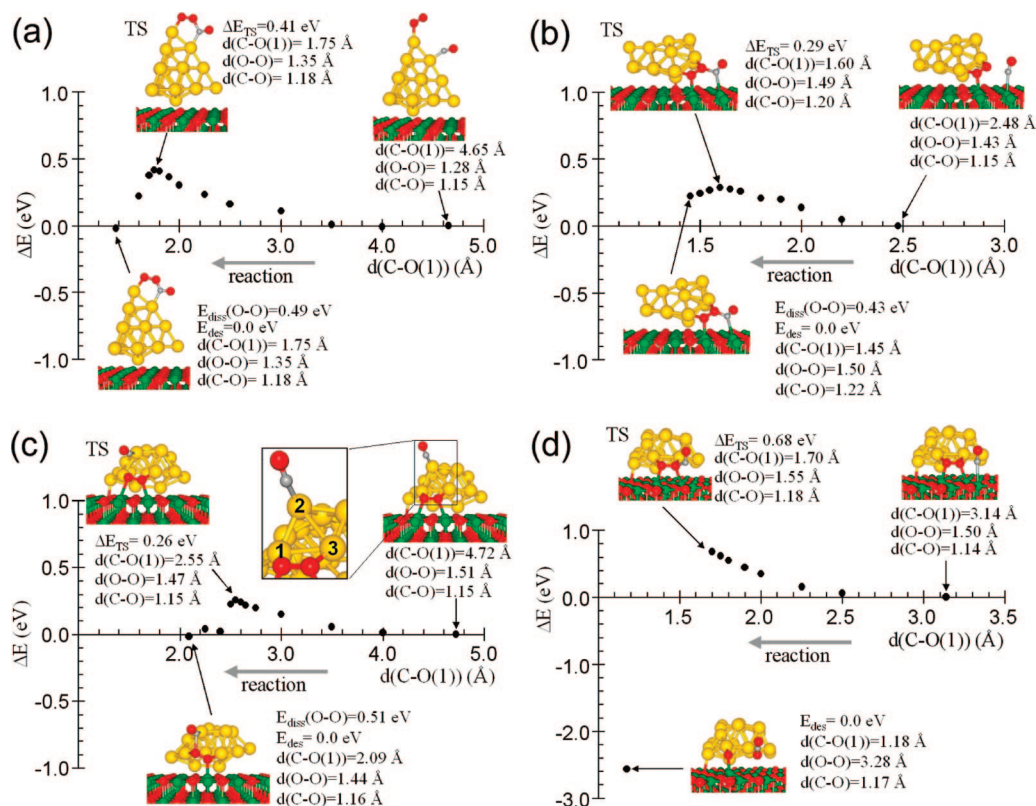
Figure 6. Reaction pathways for Au_{20} clusters adsorbed on oxygen vacancies, surface FCs, and thick MgO(100) surfaces, corresponding to the experimental data displayed in Figure 2c. (a) Reaction profile for a reaction catalyzed by a 3D tetrahedral $Au_{20}(T)$ cluster adsorbed on a single FC located under the middle of the bottom facet of the cluster, whose binding energy to the MgO surface is 4.36 eV (see Figure 3c). An O_2 molecule binds to the top apex Au atom of the $Au_{20}(T)$ cluster with a binding energy $E_B(O_2) = 0.28$ eV, and it reacts with an adsorbed CO [$E_B(CO) = 0.54$ eV], reaching a relatively low TS barrier of 0.41 eV. Dissociation of the CO–O_2 complex requires a dissociation energy $E_{diss} = 0.49$ eV, and desorption of the CO_2 product is barrierless. (b–d) Reaction pathways catalyzed by bilayer Au_{20} cluster isomers. (b) Pathway for the reaction on a bilayer isomer anchored on a single FC defect (see Figure 3d). The reaction starts from a peripherally adsorbed, peroxo-activated, O_2 molecule [$E_B(O_2) = 0.63$ eV)] and a surface-adsorbed CO molecule [$E_B(CO) = 0.29$ eV]. The TS barrier for the formation of an adsorbed CO–O_2 complex is 0.29 eV, and dissociation of the O–O bond between the complex and the other oxygen of the reactant O_2 molecule $E_{diss}(O–O) = 0.43$ eV. Desorption of the product CO_2 molecule from the surface is barrierless. (c) CO combustion reaction catalyzed by a bilayer cluster adsorbed on top of two neighboring oxygen vacancies (see Figure 3e). The reaction starts from a peripherally adsorbed [$E_B(O_2) = 0.84$ eV], peroxo-activated O_2 molecule and a CO molecule adsorbed [$E_B(CO) = 0.81$ eV] on the bilayer gold cluster. The barrier for the formation of a TS CO–O_2 complex is 0.26 eV, and the dissociation process of the complex entails an energy $E_{diss} = 0.51$ eV. Desorption of the product CO_2 molecule is found to be barrierless. In the inset, Au atoms whose positions markedly distort during the reaction (that is, exhibiting dynamic structural fluctionality) are designated as 1, 2, and 3. The distances between these atoms at various stages of the reaction are as follows: initial (rightmost) configuration, $d(1–2) = 2.95$ Å, $d(2–3) = 3.35$ Å, $d(1–3) = 3.14$ Å, and $\theta(123) = 59°$; TS configuration, $d(1–2) = 2.89$ Å, $d(2–3) = 3.11$ Å, $d(1–3) = 3.68$ Å, and $\theta(123) = 76°$; post-TS configuration (corresponding to $d[C–O(1)] = 2.09$ Å), $d(1–2) = 2.94$ Å, $d(2–3) = 3.27$ Å, $d(1–3) = 3.96$ Å, and $\theta(123) = 79°$. (d) Pathway of the reaction catalyzed by the bilayer gold cluster adsorbed on a single surface FC (as in Figure 6b), starting from a peripherally adsorbed, peroxo-activated, O_2 molecule [$E_B(O_2) = 0.96$ eV] and a surface-adsorbed CO molecule [$E_B(CO) = 0.27$ eV]. The reaction involves a TS energy barrier of 0.68 eV, and breakup of the TS complex resulting in desorption of the product CO_2 molecule occurs with no energy barrier. Color designation (online): Mg atoms in green, O atoms in red, Au atoms in yellow, and C atoms in light gray.

molecule [$E_B(O_2) = 0.96$ eV and $d(O–O) = 1.50$ Å] and a surface-adsorbed CO molecule [$E_B(CO) = 0.27$ eV] located at a distance $d[C–O(1)] = 3.14$ Å between the C atom and the nearest O atom of the adsorbed O_2 molecule. This reaction involves a TS energy barrier of 0.68 eV, and breakup of the TS complex resulting in desorption of the product CO_2 molecule occurs with no barrier.

The above examples, drawn from an ensemble of configurations corresponding to calculated reaction profiles with activation barriers in the range of about 0.35–0.75 eV, correlate well with the observed broad temperature distribution measured for the CO reaction on Au_{20} clusters deposited on thick, defect-rich MgO surfaces (Figure 2c).

Summary

The oxidation of CO on Au_{20} sensitively depends on the thickness of the MgO film grown on a Mo(100) single crystal as well as on the metal oxide stoichiometry, that is, surface

defect density. These dependencies are reflected in variations of the reaction temperatures observed in temperature-programmed desorption single-heating-cycle experiments, as well as in the amount of CO_2 produced. The first-principles theoretical investigations presented here show that the observed changes in the reactivity may be correlated, in part, with a dimensionality crossover from 3D tetrahedral Au_{20} in the case of thick films (≥ 8 ML) to 2D "wetting" planar structures for film thicknesses of less than ~3 ML; we note here that we have shown (see also the Supporting Information) through MIES and UPS measurements that these thin MgO films are highly stoichiometric; that is, they may contain only a very low number density of (Lewis-base type) oxygen vacancy (FC) defects.

Underlying the aforementioned structural and dimensionality variations is the enhanced charge transfer from the underlying Mo surface through the metal oxide occurring for the thinner films. This transferred charge accumulates mainly at the interfacial region of the adsorbed metal cluster with the metal oxide, and it stabilized

planar (wetting) configurations of the cluster (through attractive image charge interactions, which increase with the contact area of the metal cluster with the surface).[3,4] Furthermore, the excess charge can enhance the chemical catalytic activity of the adsorbed (partially charged) gold clusters (both 3D and 2D) via transfer of charge to adsorbed reactant molecules;[4] for example, activation of adsorbed O_2 through population of the $2\pi^*$ antibonding orbital and formation of a superoxo- or peroxo-activated molecule, which may react with CO in a Langmuir−Hinshelwood mechanism entailing a lower activation barrier. On the other hand, the excess interfacial charge accumulation for thin metal oxide films may enhance the binding strength of reaction intermediates and/or adsorbed product molecules, thus causing larger exit reaction barriers. Such reaction mechanisms have been illustrated in this study for both 2D and 3D Au_{20} nanoclusters adsorbed on thin MgO(1 L)/Mo(100).

For thick films and 3D Au_{20} adsorbed clusters (both tetrahedral and bilayer isomeric structures), charge accumulation, with the concomitant charging of the adsorbed clusters, can be induced by defect sites of Lewis-base character (e.g., oxygen vacancies, FCs). This charge accumulation is local, and it depends on the type of electron donor. In both cases, charging through thin metal oxide films and FC-induced charging, the excess charge is found to be located mainly on the perimeter atoms of the 2D or 3D adsorbed Au_{20} clusters; we also find that in the case of a 3D tetrahedral $Au_{20}(T)$ cluster anchored to a MgO surface FC the HOKS orbital exhibits an enhanced electronic density localized on the top apex atom of the tetrahedron. The charge accumulation defines the location of the reactive site on the cluster, and thus reactivity can be tuned as a function of the properties (thickness and stoichiometry) of the supporting metal oxide film.

We believe that the concepts and methodologies developed in this paper, and the demonstrated ability to control and tune the catalytic reactivity of gold nanoclusters through variations of the thickness and/or composition of the support [here MgO(100) grown on the surface of Mo(100)], are of importance for the development of effective gold-based nanocatalytic systems. Moreover, it will be of great interest to explore the extension of these concepts and control methods to nanocatalytic systems based on other combinations of metal nanoclusters and oxide supports.

Supporting Information Available: Experimental procedure for MgO film preparation and characterization of the film thickness and morphology by AES, He* MIES, and UPS as well as of work functions as a function of the MgO film thickness measured by UPS. This material is available free of charge via the Internet at http://pubs.acs.org.

JA804893B